IEEE Access
Multidisciplinary | Rapid Review | Open Access Journal

Received April 7, 2021, accepted April 21, 2021, date of publication April 29, 2021, date of current version May 11, 2021.

Digital Object Identifier 10.1109/ACCESS.2021.3076432

Molecular Imaging of Pulmonary Tuberculosis in an Ex-Vivo Mouse Model Using Spectral Photon-Counting Computed Tomography and Micro-CT

CHIARA LOWE[1], ANA ORTEGA-GIL[2,3], MAHDIEH MOGHISEH[1,4], NIGEL G. ANDERSON[1], ARRATE MUÑOZ-BARRUTIA[2,3], JUAN JOSÉ VAQUERO[2,3], (Senior Member, IEEE), AAMIR Y. RAJA[1,4,5], AYSOUDA MATANAGHI[1], ALEXANDER I. CHERNOGLAZOV[4,6], THEODORUS DAPAMEDE[1], SIKIRU A ADEBILEJE[1,6], STEVEN ALEXANDER[4], MAYA R. AMMA[1], MARZIEH ANJOMROUZ[4], FATEMEH ASGHARIOMABAD[1], ALI ATHARIFARD[4], JAMES ATLAS[7], KENZIE BAER[1], STEPHEN T. BELL[4], SRINIDHI BHEESETTE[1,4,8], PHILIP H. BUTLER[1,4,6,7,8], PIERRE CARBONEZ[1,8], CLAIRE CHAMBERS[7], KRISHNA M. CHAPAGAIN[1], JENNIFER A. CLARK[9], FRANCES COLGAN[1], JONATHAN S. CRIGHTON[1], SHISHIR DAHAL[1,10,11], JÉRÔME DAMET[1,8,12], NIELS J. A. DE RUITER[1,4,6,7], ROBERT M. N. DOESBURG[4], NERYDA DUNCAN[7], NOOSHIN GHODSIAN[7], STEVEN P. GIESEG[1,7,8], BRIAN P. GOULTER[4], SAM GURNEY[1], JOSEPH L. HEALY[4], PRAVEEN KUMAR KANITHI[6,7], TRACY KIRKBRIDE[9], STUART P. LANSLEY[4,8], V. B. H. MANDALIKA[4,6,7], EMMANUEL MARFO[1], DAVID PALMER[13], RAJ K. PANTA[1,4,8], HANNAH M. PREBBLE[4], PETER RENAUD[1,7], YANN SAYOUS[7], NANETTE SCHLEICH[14], EMILY SEARLE[7], JEREENA S. SHEEJA[7], LIEZA VANDEN BROEKE[4], VIVEK V. S.[4], E. PETER WALKER[1], MICHAEL F. WALSH[4], MANOJ WIJESOORIYA[7], W ROSS YOUNGER[4], AND ANTHONY P. H. BUTLER[1,4,7,8]

[1]Department of Radiology, University of Otago Christchurch, Christchurch 8011, New Zealand
[2]Departamento de Bioingeniería e Ingeniería Aeroespacial, Universidad Carlos III de Madrid, 28903 Getafe, Spain
[3]Instituto de Investigación Sanitaria Gregorio Marañón (IiSGM), 28007 Madrid, Spain
[4]MARS Bioimaging Ltd., Christchurch 8011, New Zealand
[5]Department of Physics, Khalifa University, Abu Dhabi, United Arab Emirates
[6]Human Interface Technology Laboratory New Zealand, University of Canterbury, Christchurch 8041, New Zealand
[7]Department of Physics, University of Canterbury, Christchurch 8041, New Zealand
[8]European Organization for Nuclear Research (CERN), 1211 Geneva, Switzerland
[9]Ara Institute of Canterbury, Christchurch 8011, New Zealand
[10]Ministry of Health, Kathmandu 44600, Nepal
[11]National Academy of Medical Sciences, Kathmandu 44600, Nepal
[12]Institute of Radiation Physics, Lausanne University Hospital, 1011 Lausanne, Switzerland
[13]Department of Wine, Food and Molecular Biosciences, Lincoln University, Lincoln 7647, New Zealand
[14]Department of Radiation Therapy, University of Otago, Wellington 6242, New Zealand

Corresponding author: Mahdieh Moghiseh (mahdieh.moghiseh@marsbioimaging.com)

This work was supported in part by the Ministry of Business, Innovation and Employment (MBIE), New Zealand, under Contract UOCX1404, in part by MARS Bioimaging Ltd., in part by the Ministry of Education through the MedTech CoRE, in part by the University of Otago, in part by the Instituto de Salud Carlos III (Plan Estatal de I+D+i 2013–2016), in part by the European Social Fund (ESF) (ESF investing in your future), in part by the Innovative Medicines Initiative Joint Undertaking through the European Union Seventh Framework Program (FP7/2007–2013) under Grant 115337 and Grant 853989, in part by the European Federation of Pharmaceutical Industries and Associations (EFPIA) Companies, in part by the Spanish Ministry of Economy under Project TEC2016-78052-R, and in part by the Spanish Ministry of Science and Innovation under Grant PID2019-109820RB-I00.

ABSTRACT Assessment of disease burden and drug efficacy is achieved preclinically using high resolution micro computed tomography (CT). However, micro-CT is not applicable to clinical human imaging due to operating at high dose. In addition, the technology differences between micro-CT and standard clinical CT prevent direct translation of preclinical applications. The current proof-of-concept study presents spectral photon-counting CT as a clinically translatable, molecular imaging tool by assessing contrast uptake in

The associate editor coordinating the review of this manuscript and approving it for publication was Yizhang Jiang.

an *ex-vivo* mouse model of pulmonary tuberculosis (TB). Iodine, a common contrast used in clinical CT imaging, was introduced into a murine model of TB. The excised mouse lungs were imaged using a standard micro-CT subsystem (SuperArgus) and the contrast enhanced TB lesions quantified. The same lungs were imaged using a spectral photon-counting CT system (MARS small-bore scanner). Iodine and soft tissues (water and lipid) were materially separated, and iodine uptake quantified. The volume of the TB infection quantified by spectral CT and micro-CT was found to be 2.96 mm^3 and 2.83 mm^3, respectively. This proof-of-concept study showed that spectral photon-counting CT could be used as a predictive preclinical imaging tool for the purpose of facilitating drug discovery and development. Also, as this imaging modality is available for human trials, all applications are translatable to human imaging. In conclusion, spectral photon-counting CT could accelerate a deeper understanding of infectious lung diseases using targeted pharmaceuticals and intrinsic markers, and ultimately improve the efficacy of therapies by measuring drug delivery and response to treatment in animal models and later in humans.

INDEX TERMS High resolution, translatable molecular imaging, photon-counting spectral CT, pulmonary tuberculosis, micro-CT.

I. INTRODUCTION

According to the World Health Organization, *mycobacterium tuberculosis* (TB) is a worldwide health problem, with 10 million new TB cases and 1.3 million deaths recorded in 2019 alone [1]. Drug-resistant TB strains remain a public health crisis threat and account for 3.3% of TB-related deaths [2]–[4]. Extensive efforts to curb TB and TB drug resistance via novel therapies have resulted in a decline in TB incidence of approximately 2% per year. However, decreasing incidence rates must accelerate in order to reach targets set by the Sustainable Development Goals (SDG) [1].

Clinical trials examining new TB treatments are lengthy and complex, suffer from poor patient compliance, and require long periods of follow-up to assess the patient's response to treatment [1], [5], [6]. Therefore, uncertainty surrounding the optimal combination of drugs and doses to effectively treat patients is a major cause of efficacy assessment failure [5], [6]. Consequently, predictive preclinical imaging plays a vital role in facilitating the development of novel drug regimens and preclinical efficacy studies using animal models of disease is key to supporting the rationale of clinical trials involving patients [7].

Micro-CT is widely used in preclinical laboratories for non-invasive, high-resolution anatomical imaging in animal models of disease [8], [9]. Micro-CT can provide insights into new applications for clinical CT. However, micro-CT is limited by the associated high radiation dose and technology differences. In other words, scaling up micro-CT to human imaging would result in harmful exposure levels, therefore, preventing direct translation of micro-CT findings to clinical CT [8], [9]. Furthermore, A relatively large number of subjects and sacrifices at each time point are necessary, imposing constraints on the ethical feasibility and efficacy of such preclinical investigations. Moreover, pharmacodynamic (PD) endpoints in preclinical investigations (involving animal models) are commonly expressed as proportions of *in-vitro* culture negative at a limited number of time points [10]–[12]. These results do not reflect outcomes in humans due to the variability in the level of bacillary replication and recurrence induced by non-standardized experimental conditions [11].

Preclinical imaging that uses the same technologies, in terms of hardware and software, as for clinical imaging would result in a more rapid translation [12]–[14]. Thus, spectral photon-counting (CT) should be considered as a translatable technique.

Spectral photon-counting CT is an advanced technique that increases contrast resolution in soft-tissue using novel properties of a photon-counting detector [13], [15]. The spectral scanner employed in this study is the MARS spectral CT system (MARS-11 V5.1 (2016) S/N:11, MARS Bioimaging Ltd, New Zealand), which is equipped with the Medipix3RX photon-counting detector [17], [18]. The Medipix3RX detector developed at CERN (The European Organization for Nuclear Research) comprises a cadmium zinc telluride semiconductor sensor layer, plus readout electronics for measuring up to eight energies at high resolution (50-200 μm). Three counters operate in single pixel mode, one counter is an arbitration counter, and four energy counters operate in charge summing mode (CSM). CSM refers to communication between pixels, where an incidental charge cloud spread over neighboring pixels is summed and allocated to the pixel that registered the highest charge. This technique minimizes the effect of charge sharing when using very small pixels (110 μm), which improves energy and spatial resolution [19]. The four counters operating in CSM were used in the current study. Photon energy measurements, combined with known attenuation energy dependence in different materials, result in the simultaneous differentiation and quantification of up to six materials [15], [20]. Spectral photon-counting CT imaging with the MARS scanner has proven useful in a wide range of preclinical applications pertinent to common human conditions, including crystal arthropathies [21], atherosclerosis [22], bone health [23]–[25], and cancer [26], [27]. Studies have also used MARS spectral imaging to investigate novel targeted pharmaceuticals, such as hafnia-based nanoparticles that have been chemically trained to highlight bone microdamage [23], [26].

To demonstrate how spectral photon-counting CT can facilitate drug dose optimization via molecular imaging, an iodine-based contrast agent was administered to a murine

model of TB and scanned using a spectral photon-counting CT scanner. Iodine was chosen because it is an easily accessible, standard X-ray imaging contrast agent. Measurement of the healthy and disease-related lung tissue volume by the spectral CT was compared to quantification performed on the same lungs by high-resolution micro-CT subsystem (SuperArgus scanner, Sedecal Molecular Imaging Madrid), optimized for soft-tissue imaging tasks [28]. Spectral photon-counting scanners provide human translatable preclinical molecular imaging, simultaneous measurements of multiple materials, the potential for the non-invasive assessment of PD endpoints, and higher energy and spatial resolution at greater sensitivity. This proof-of-concept study is the first step in being able to diagnostically target TB lung infection and quantify drug delivery. The unique properties of photon-counting technology combined with a high-Z contrast material attached to a biomarker and/or anti-TB drug will enable molecular imaging that could facilitate drug development.

TABLE 1. Summary of acquisition parameters for pulmonary task using MARS-11 (V5.1 (2026) S/N:11) and Micro-CT subsystem of super argus.

Parameter	MARS spectral CT	SuperArgus micro-CT
Scan type	continuous motion	step and shoot
Tube voltage	60 kVp	69 kVp
Tube current	90 uA	420 uA
Exposure time	220 ms	50 ms
Magnification	1.25	3.1
Field of view	32 mm diameter	93.1 x 58.9 mm
Circular projections, Flat fields	720, 720	514, 514
Voxel (isotropic)	0.09 mm	0.088 mm
X-ray filtration	3.8 Al (2 mm Al + 1.8 mm Al intrinsic)	0.2 mm Cu + 1.8 mm Al intrinsic
Energies	20-27, 27-34, 34-45, and 45-60 keV	20-60 keV
Acquisition time	30 min	7 min
Detector model	Medipix3RX	Dexela 1512
Reconstruction algorithm	mars_recon	FDK cone beam analytic

II. MATERIALS AND METHODS

A. LUNG SAMPLE PREPARATION

The current research was based on excised whole organs from procedures approved by the Animal Experimentation Ethics Committee of Hospital General Universitario Gregorio Maran, Madrid, Spain and performed according to EU directive 2010/63/EU and national regulations (RD 53/2013).

The mouse lung tissue examined were from two females of the C57BL/6J strain. One mouse was inoculated with virulent TB H37Rv strain via exposure to aerosol infection (dose 100 colony forming units) at the age 8-12 weeks. Both animals were euthanized eight weeks following the intra-tracheal insult using CO_2 gas. At that time, chronic TB was established, and well-formed lesions were present (animals were euthanized prior to the development of calcification). Prior to lung tissue extraction, the animals received 15 mL of 10% formalin through the trachea. To retain the formalin solution within the lungs, a thoracic opening was made, and the lungs were closed at the top and bottom by a thread. Once fixed, the lungs were extracted and placed into 10% formaldehyde for at least 18 days to ensure deactivation of the TB infection.

B. LUNG SAMPLE STAINING

The tissue samples underwent a fixation procedure (graded ethanol concentration fixation: GECF) prior to staining with contrast. The purpose of the GECF protocol, described in [29], was to increase the absorption of contrast. One healthy mouse lung and one TB-infected lung were immersed in iodine (I_2; Sigma-Aldrich Co.) in a 3% w/v ethanol solution for 2 hours. The lungs were kept inflated at a constant pressure of 20 cm H_2O during the GECF and staining processes to prevent abrupt shrinkage and ensure homogeneous uptake. Following the staining process, the lungs were fixed in paraffin. Paraffin fixation provides the opportunity to cut the lungs for histological examination. A tinfoil layer was used to cover the bottom of the paraffin cassette measuring 5 cm (w) x 7 cm (l) x 1.5 cm (d). A total of 104 mL of heated paraffin was used to embed the TB-infected and healthy lung samples separately. Paraffin blocks were left to cool and harden for 24 hrs before imaging. The purpose of paraffin fixing was to enable a direct comparison between micro-CT and spectral CT images [30].

C. LUNG IMAGING

A summary of the imaging protocols employed for the micro-CT (SuperArgus scanner, Sedecal Molecular Imaging Madrid) and spectral CT (MARS-11 scanner V5.1 (2016) S/N:11, MARS Bioimaging Ltd, New Zealand) are shown in Table 1. The acquisition protocol for the micro-CT was optimized (in terms of beam conformation) for enhanced soft-tissue contrast [10]. The micro-CT is based on an energy-integration detector therefore has one energy range. Pulmonary imaging tasks required copper filtration with a peak voltage of 65∼70 kVp. Given that this protocol is also used for *in-vivo* imaging, a compromise between image resolution and total acquisition time was taken into consideration.

For an equivalent acquisition protocol to that of the micro-CT, the spectral CT X-ray source tube was operated at a constant peak voltage of 60 kVp and the tube current increased to 90 μA, with 3.8 mm total aluminum X-ray beam filtration. Energy thresholds were appropriately selected to perform material decomposition (MD) of iodine, a second high-Z contrast (silver nitrate), and soft tissues (water and lipid). Silver nitrate was included in this phantom for a distinguishing point. Protocol optimization for the simultaneous differentiation of iodine and silver in a calibration phantom and lung tissue samples (in ethanol) is supplied in the supplementary material. Four energy bins in CSM were used. The energy thresholds selected were: 20, 27, 34, and 45 keV. Material calibration provides protocol-specific detector responses (spectral and linearity responses) that enable accurate identification and quantification of the calibrated

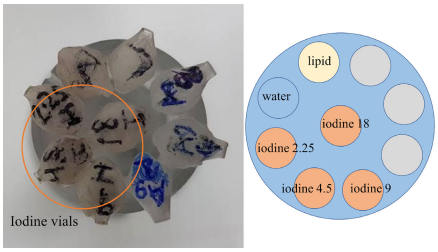

FIGURE 1. ***Left*: Picture of the PMMA calibration phantom containing 200 μL Eppendorf tubes of iodine solutions (2.25, 4.5, 9, and 18 mg/mL), lipid (L), water (W), and silver nitrate solutions (2, 4, and 8 mg/mL). Silver nitrate was included in this phantom for imaging for a distinguishing point. Protocol optimization for the simultaneous differentiation of iodine and silver in a calibration phantom and lung tissue samples (in ethanol) is supplied in the supplementary material. *Right*: A schematic of the calibration phantom.**

materials. A PMMA (Polymethyl methacrylate) calibration phantom containing 200 μL vials of water, lipid, and iodine-based solutions (2.25, 4.5, 9, and 18 mg/mL) was scanned. The calibration phantom is shown in Fig. 1. The mass attenuation values were obtained from analysis of the calibration phantom vials using an in-house program [31], [32]. MD was applied to the reconstructed linear attenuation volumes for each energy window of the phantom vials and excised lungs. The performance of the MD step was assessed by measuring material identification and quantification success of the iodine vials.

D. TISSUE ANALYSIS

Segmentation of the lung damage caused by the TB infection in standard PET/CT and CT images is performed using thresholding methods, such as that described in [33]. This method uses an automated algorithm that extracts the volume of the damaged lung tissue using Hounsfield Unit (HU) values that reveal abnormal densities associated with disease. A similar thresholding methodology was later applied in [34], where accurate CT segmentation of the disease-associated tissue could be aided using histological analysis.

For this study, histograms of the lung voxels in HU (micro-CT) or iodine concentration (spectral CT) were exported for the healthy lung. The greatest density (HU) or concentration (mg/mL) within the healthy lung dataset was found. For micro-CT, a 5% margin of error, established by [34], was added and the new HU value was used as the threshold between healthy and disease-related lung tissue. For spectral CT, the variation in measured iodine concentration (Fig. 7) was assessed. A positive linear relationship ($r = 0.98$) was found between iodine concentration and standard error. The positive linear relationship was used to find the standard error at the concentration of iodine that separated healthy and disease-related tissue (24.4 mg/mL). The calculated standard error was added to this threshold. Table 2 provides a summary of the thresholding values used to segment the background, healthy tissue, and disease-related tissue for quantification measurements by photon-counting CT and by micro-CT. Lung volumes were calculated by summing the volume of voxels whose values fell within the established thresholds.

TABLE 2. Thresholds for tissue segmentation.

	MARS spectral CT (mg/mL)	SuperArgus Micro-CT (HU)
Background	< 0	< -70
Healthy tissue	0 < 27.8 (24.4 + 3.4 margin)	-70 < 2943 (2803 + 5% margin)
TB-infected tissue	27.8 < 36.2	2943 < 3096

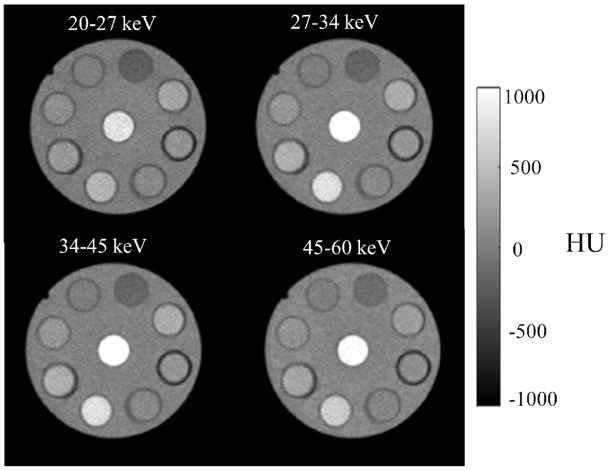

FIGURE 2. **MARS energy images in HU of the phantom detailed in Fig. 1 for each energy bin.**

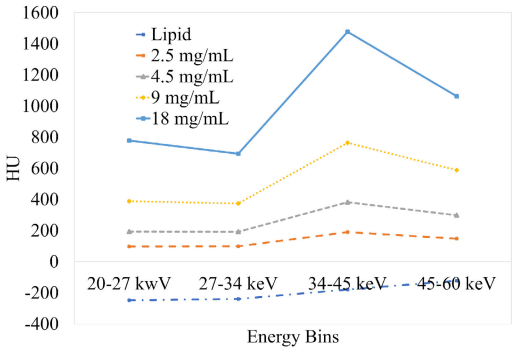

FIGURE 3. **Spectral response of the detector for iodine calibration phantom vials and lipid. Enhancement of attenuation is observed (for all iodine concentrations) in energy bin three (34-45 keV), which indicates the K-edge of iodine. The standard errors for each data point are in the range of 1-10 HU.**

III. RESULTS

A. MARS SPECTRAL CT CALIBRATION PHANTOM ANALYSIS

Fig. 2 shows one reconstructed slice of the calibration phantom in each energy bin. The unique spectral response for the iodine calibration vials and lipid are included in Fig. 3. The K-edge of iodine was detected as a peak in attenuation in the third energy bin (34-45 keV) for every concentration. Fig. 4 displays the measured linearity of attenuation in each energy bin for the iodine solution.

Fig. 5 illustrates the detection of iodine in the iodine-based solutions, water, lipid, and the second high-Z contrast

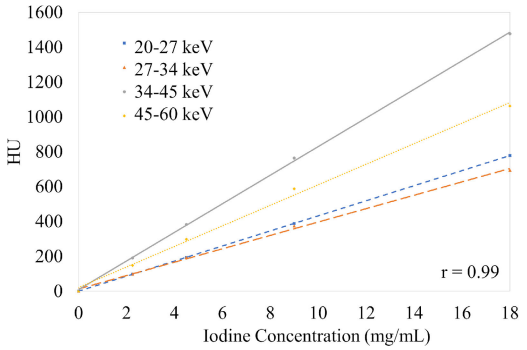

FIGURE 4. The linearity of attenuation for iodine is established via the calibration phantom. Linear regression lines are displayed on the graph. $r^2 = 0.99$ for all energy bins. The standard errors for each data point are in the range of 2-6 HU.

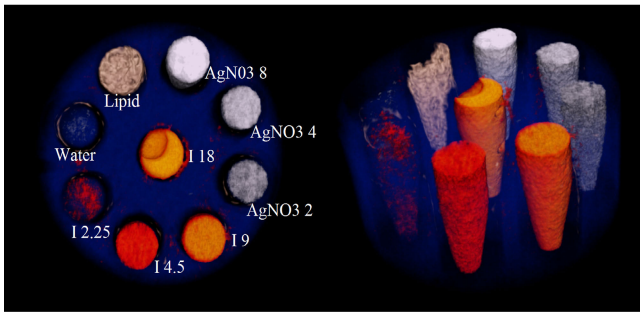

FIGURE 5. Material decomposition of the PMMA calibration phantom views using MARS Vision (in-house visualization software). Four datasets shown: iodine (orange), lipid (beige), silver nitrate (white), and water (semi-transparent blue).

material for a distinguishing point. Iodine identification success is greater than 99.5% for all iodine concentrations. That is, 99.5% of voxels within the iodine vials were correctly identified as iodine. An identification success of 80% or greater is considered good material decomposition performance [32].

Each calibration vial was quantified in the MD and compared to the actual known concentration, as shown in Fig. 6. The comparison provides validation regarding iodine measured in the lungs. In addition, the margin of error for tissue segmentation using the spectral CT data was established using the quantification data (see methods). The linearity of attenuation was established in each energy bin, thus, the measured iodine presented comparable results. This provides confidence that the stained concentration (in the lung samples) and concentration measured using the spectral CT will be comparable.

B. MARS SPECTRAL CT VS SUPERARGUS MICRO-CT

Due to the whole organ uptake of iodine, the iodine concentration was normalized to 0 mg/mL. The threshold between healthy tissue and background was considered 0 mg/mL of iodine (Table 2).

Using in-house visualization software (MARS Vision), Fig. 7 displays three-dimensional (3D) data obtained by

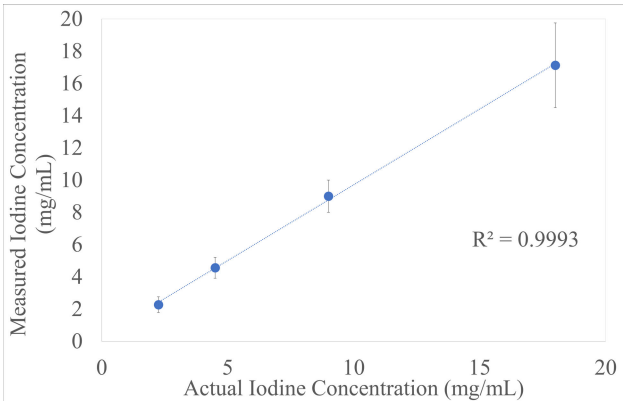

FIGURE 6. Measured concentration from MARS MD on the y-axis and the known concentration on the x-axis. Iodine shows comparable values; therefore, we can be confident that what is measured in the biological specimen will be comparable to what is present in the organ. Variance shown.

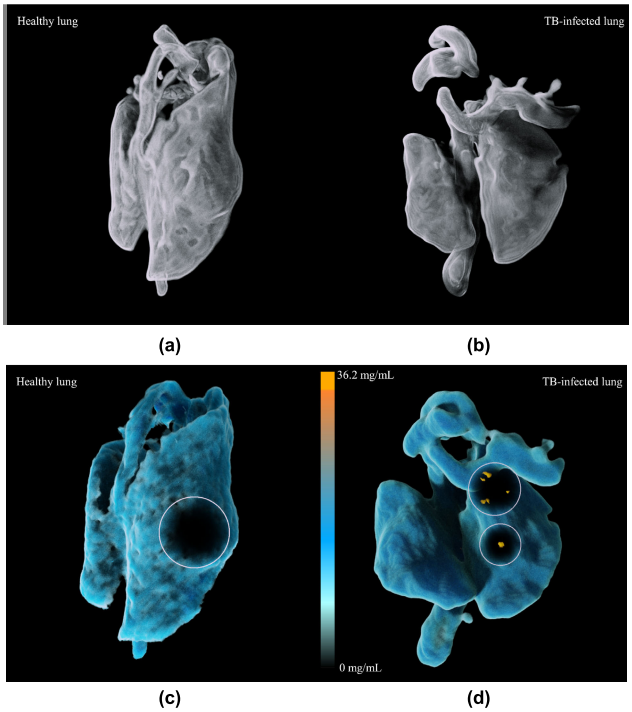

FIGURE 7. Visualization using MARS Vision was performed. (a) Micro-CT energy data of healthy lung and (b) TB-infected lung used HU values and thresholds shown in Table 2 to visualize the lungs. (c) The water channel and iodine channel with thresholds applied shows the healthy lung with no iodine above 27.8 mg/mL. The magic lens tool reveals one region of interest. However, it is important to note there is no iodine present <27.8 mg/mL throughout the lung, there are no lesions. (d) Similarly, the water channel and iodine channel show the TB-infected lung. The lesions can be viewed using the magic lens which removes the water channel in a region of interest. The lipid channel is not shown since concentration was measured to be zero (no fat within the mouse lungs as expected).

the micro-CT (top) and data obtained by the spectral CT (bottom). There was some collapse of lung tissue due to the paraffin fixing process [30]. The threshold computed for tissue analysis was applied to the iodine material dataset of the healthy and TB-infected lung images. The result is

no iodine was visualized in the healthy lung, as shown by the MARS Vision magic lens tool in Fig. 7c. The magic lens tool is used to remove one or more material channels. In this case, the water channel is removed to observe the highest concentrations of iodine. Iodine concentration above the threshold that is visualized in the TB-infected lung is associated with disease-related tissue (orange). Higher concentrations of iodine helped locate TB lesions and quantify infection.

The healthy lung volume was quantified: 44.6 mm^3 and 49.7 mm^3 for the spectral CT and micro-CT, respectively. The TB-infected lung was quantified: healthy tissue was found to be 38.18 mm^3 and 47.24 mm^3 for the spectral CT and micro-CT, respectively. The volume of disease-related tissue was found to be 2.96 mm^3 and 2.83 mm^3 for the spectral CT and micro-CT, respectively.

Histology provides the ground truth to check for correlation between images and histological cuts. The methods we followed for guiding histology are well established [28], [30], [35]. The results of the histological images confirmed lesion location. That is, our expert confirmed that the lesions located by spectral CT and micro-CT were visualized in histology. Also, lesions were not found in the healthy (control) lung tissue. Histological slides are available in the supplementary material.

IV. DISCUSSION

The current research documented the first-time spectral photon-counting CT imaging of contrast-enhanced TB lesions as a way of illustrating cutting-edge human translational, preclinical molecular imaging. This study compared the results from spectral photon-counting CT (MARS spectral CT) with micro-CT (SuperArgus). The total volume of the healthy and disease-related lung tissue quantified by spectral CT was comparable to the volume quantified by micro-CT. Differences in tissue volume was due to using different methodology to provide margins of error for each modality. For micro-CT, a 5% margin was established by previous research which examined multiple healthy lung tissue samples [34]. For the spectral CT, only one healthy lung tissue iodine dataset was available. Therefore, a margin of error relating to the variation in measured iodine from the calibration vials was calculated and added. The volume of tissue calculation is sensitive to the margin of error; thus, future experiments should scan multiple healthy lung samples with MARS to obtain a material-specific and statistically relevant margin of error. This technique could further optimize thresholding of spectral CT data and reduce differences in the measurements. The current study was a proof-of-concept, thus multiple samples were not scanned. Another possible reason for the difference in the measurements between spectral CT and micro-CT is misidentification of materials; lipid or paraffin wax misidentified as water or soft tissue. MARS MD algorithm employs a constrained linear least squares method, which is applied in the image domain using the mass attenuation coefficient values from the calibration phantom [36]. Future MD algorithms will be improved by using a joint reconstruction process (not limited to either projection- or image-domain) and if deep learning can be incorporated [37], [38].

Traditional diagnostic modalities employed for TB include microbiology, microscopy, and molecular techniques (nucleic acid test or acid-fast staining), all of which require biological samples (blood, stool, or sputum cultures) [39]. Biological samples may not accurately reflect the local biology at the site of infection, thus, are often not sensitive enough as a stand-alone diagnostic test (poor sensitivity: 45-85%) [35], [40]. Furthermore, the requirement of sputum cultures limits or delays diagnosis because TB bacterium is difficult and slow to cultivate *ex-vivo* (2-8 weeks) [41]. Biopsies (removal of tissue) are often the last resort for unequivocal diagnosis. However, biopsies are invasive, generally limited to the most accessible lesion, prone to sampling error, and fail to capture the heterogeneous nature of TB infection. Thus, like biological samples, biopsies provide a localized indication of lesion composition, they do not report on the entire disease. Clinically available imaging modalities can provide whole tissue assessment and have a role depending on the patient's clinical profile. X-ray imaging is based on anatomical changes; changes that are often delayed relative to disease progression at the molecular level. Spectral photon-counting CT provides more information in the form of tissue characterization, as well as density. The benefit of spectral CT also comes from its ability to be directly translated to clinical human imaging. MARS preclinical systems use almost the same technology, in terms of hardware and software, as MARS clinical systems, which are currently being used for human trials.

Bacterial-specific imaging is an active area of preclinical research with encouraging results. The goal is to provide non-invasive whole-body analysis using bacteria-specific imaging probes. Patient outcomes could be significantly improved by fast identification of infection and monitoring of disease response to treatment. Several radio-labelled derivatives of antibiotics for PET imaging have been investigated [42]–[44]. For PET, the selective metabolism of small molecules, such as sugar, for differentiating bacterial infections from non-infectious processes has been examined [43]. Unlike PET, spectral CT does not require radioactive tracers for molecular imaging. Therefore, the authors see the next step in taking this proof-of-concept to actual application is imaging a non-radioactive, high-Z atom functionalized by a key biomarker of TB and/or TB-specific drug. Spectral photon-counting CT could enable a more sensitive and specific research tool. Functionalized or labelled high-Z nanoparticles with spectral CT has been demonstrated [23], [26]. Disease severity, disease heterogeneity, and drug delivery could be measured [26].

With regards to drug development, translational research using preclinical micro-CT plays a pivotal role in the management of TB, by assessing disease severity and evaluating new effective anti-tuberculosis drug combinations for therapy [35], [45], [46]. Micro-CT offers high resolution, low

cost, and wide availability. Intensity histograms in HU are used to provide tissue characterization, since diseased tissue present abnormal densities in the organ of interest [32], [45], [47]. Soft-tissue imaging, however, is limited, and characterization of abnormal X-ray densities associated with TB is highly challenging in preclinical research [8], [9]. Contrast material can be employed to enhance attenuation and assist in 3D visualization of soft tissue and lesion composition.

Another potential advantage of spectral CT imaging includes the reduction of biological variability (each animal is utilized as its own control), acquiring data non-invasively, repeated imaging if needed (non-toxic contrast should be used), and a reduction in the number of animals required for a study. Current micro-CT uses high tube currents which limit the use of animals in longitudinal studies [9]. Future studies can use MARS spectral photon-counting CT to perform longitudinal quantitative imaging that can be collected from the same animal with low dose [48], and thus subtle functional changes and development of structural changes over time can be identified. To improve the current proof-of-concept study and take our work a step closer to actual application, we recommend future investigations compare contrast uptake by TB lesions versus non-TB lung masses. This would demonstrate the ability to distinguish TB lesions from non-TB nodules, using spectral photon-counting CT. In addition, we recommend imaging of functionalized pharmaceuticals specific to pulmonary TB to measure drug delivery and test the effectiveness of the targeting methods used. More precise diagnosis, monitoring of therapy efficacy, and the development of new and more effective drugs could be key to the eradication of TB.

V. CONCLUSION

The results of this study support the idea that photon-counting CT imaging is capable of molecular imaging when enhanced by high-Z pharmaceuticals. The Medipix3RX detector operating four CSM energy bins provided sufficient spectral information for the simultaneous differentiation of iodine, water, and lipid (and a second high-Z contrast). In an *ex-vivo* mouse model of chronic TB, detection of iodine contrast enabled segmentation and volume quantification of healthy and disease-related lung tissue. The results demonstrated the potential clinical utility of photon-counting CT imaging for molecular imaging in infectious lung diseases. In the future, if a TB-specific drug were to be incorporated with a high-Z nanoparticle, spectral CT could provide non-invasive evaluation of drug delivery and response to treatment. Such an imaging platform would have the potential to assist diagnosis and accelerate the development of novel therapies, which is essential for the eradication of TB.

Photon-counting CT technology offers improved spatial and energy resolution. Thus, it is a promising next step in the evolution of CT.

ACKNOWLEDGMENT

The authors would like to acknowledge the Medipix2, Medipix3, and Medipix4 collaborations. They would also like to take this opportunity to acknowledge the generous support of the MARS Collaboration. They would also like to acknowledge Dr. Guembe from CIMA-Universidad de Navarra for preparing and staining the tissue sections.

REFERENCES

[1] World Health Organization. (2020). *Global Tuberculosis Report*. Accessed: Jun. 15, 2020. [Online]. Available: https://www.who.int/tb/publications/global_report/en/

[2] C. Dye, "Global epidemiology of tuberculosis," *Lancet*, vol. 367, no. 9514, pp. 938–940, Mar. 2006.

[3] C. Dye, S. Scheele, V. Pathania, and M. C. Raviglione, "Global burden of tuberculosis: Estimated incidence, prevalence, and mortality by country," *J. Amer. Med. Assoc.*, vol. 282, no. 7, pp. 677–686, 1999.

[4] N. S. Shah, R. Pratt, L. Armstrong, V. Robison, K. G. Castro, and J. P. Cegielski, "Extensively drug-resistant tuberculosis in the United States, 1993–2007," *J. Amer. Med. Assoc.*, vol. 300, no. 18, pp. 2153–2160, 2008.

[5] TB Alliance. (2020). *Inadequate Treatment*. Accessed: Jun. 15, 2020. [Online]. Available: https://www.tballiance.org/why-new-tb-drugs/inadequate-treatment

[6] P. R. Shankar, "Book review: Tackling drug-resistant infections globally," *Arch. Pharmacy Pract.*, vol. 7, no. 3, pp. 110–111, 2006.

[7] R. Willmann, J. Lee, C. Turner, K. Nagaraju, A. Aartsma-Rus, D. J. Wells, K. R. Wagner, C. Csimma, V. Straub, M. D. Grounds, and A. De Luca, "Improving translatability of preclinical studies for neuromuscular disorders: Lessons from the TREAT-NMD advisory committee for therapeutics (TACT)," *Disease Models Mech.*, vol. 13, no. 2, Feb. 2020, Art. no. dmm042903.

[8] E. L. Ritman, "Small-animal CT: Its difference from, and impact on, clinical CT," *Nucl. Instrum. Methods Phys. Res. A, Accel. Spectrom. Detect. Assoc. Equip.*, vol. 580, no. 2, pp. 968–970, Oct. 2007.

[9] D. P. Clark and C. T. Badea, "Micro-CT of rodents: State-of-the-art and future perspectives," *Phys. Medica*, vol. 30, no. 6, pp. 619–634, Sep. 2014.

[10] R. J. Basaraba, "Experimental tuberculosis: The role of comparative pathology in the discovery of improved tuberculosis treatment strategies," *Tuberculosis*, vol. 88, pp. S35–S47, Aug. 2008.

[11] A. J. Lenaerts, M. A. DeGroote, and I. M. Orme, "Preclinical testing of new drugs for tuberculosis: Current challenges," *Trends Microbiol.*, vol. 16, no. 2, pp. 48–54, Feb. 2008.

[12] R. J. Cohrs, T. Martin, P. Ghahramani, L. Bidaut, P. J. Higgins, and A. Shahzad, "Translational medicine definition by the European society for translational medicine," *Eur. J. Mol. Clin. Med.*, vol. 2, no. 3, p. 86, Dec. 2014.

[13] D. M. Rubio, E. E. Schoenbaum, L. S. Lee, D. E. Schteingart, P. R. Marantz, K. E. Anderson, L. D. Platt, A. Baez, and K. Esposito, "Defining translational research: Implications for training," *Academic Med. Colleges*, vol. 85, no. 3, pp. 470–475, Mar. 2010.

[14] M. F. Fiordelisi, C. Cavaliere, L. Auletta, L. Basso, and M. Salvatore, "Magnetic resonance imaging for translational research in oncology," *J. Clin. Med.*, vol. 8, no. 11, p. 1883, Nov. 2019.

[15] E. R. Driver, G. J. Ryan, D. R. Hoff, S. M. Irwin, R. J. Basaraba, I. Kramnik, and A. J. Lenaerts, "Evaluation of a mouse model of necrotic granuloma formation using C3HeB/FeJ mice for testing of drugs against mycobacterium tuberculosis," *Antimicrobial Agents Chemotherapy*, vol. 56, no. 6, pp. 3181–3195, Jun. 2012.

[16] R. Aamir *et al.*, "MARS spectral molecular imaging of lamb tissue: Data collection and image analysis," *J. Instrum.*, vol. 9, no. 2, 2014, Art. no. P02005.

[17] P. H. Butler *et al.*, "MARS pre-clinical imaging: The benefits of small pixels and good energy data," *Proc. SPIE*, vol. 11113, Sep. 2019, Art. no. 111130C.

[18] MARS Bioimaging. (2020). *Home*. Accessed: Jun. 15, 2020. [Online]. Available: https://www.marsbioimaging.com/

[19] R. Panta *et al.*, "First human imaging with MARS photon-counting CT," in *Proc. IEEE Nucl. Sci. Symp. Med. Imag. Conf. (NSS/MIC)*, Nov. 2018, pp. 1–7.

[20] M. Moghiseh, R. Aamir, R. K. Panta, N. de Ruiter, A. Chernoglazov, J. L. Healy, A. P. Butler, and N. G. Anderson, "Discrimination of multiple high-Z materials by multi-energy spectral CT—A phantom study," *JSM Biomed. Imag. Data Paper*, vol. 61, p. 1007, Nov. 2016.

[21] L. K. Stamp, N. G. Anderson, F. Becce, M. Rajeswari, M. Polson, O. Guyen, A. Viry, C. Choi, T. E. Kirkbride, and A. Y. Raja, "Clinical utility of multi-energy spectral photon-counting computed tomography in crystal arthritis," *Arthritis Rheumatol.*, vol. 71, no. 7, pp. 1158–1162, 2019.

[22] T. E. Kirkbride, A. Y. Raja, K. Müller, C. J. Bateman, F. Becce, and N. G. Anderson, "Discrimination between calcium hydroxyapatite and calcium oxalate using multienergy spectral photon-counting CT," *Amer. J. Roentgenol.*, vol. 209, no. 5, pp. 1088–1092, Nov. 2017.

[23] F. Ostadhossein, I. Tripathi, L. Benig, D. LoBato, M. Moghiseh, C. Lowe, A. Raja, A. Butler, R. Panta, M. Anjomrouz, A. Chernoglazov, and D. Pan, "Multi 'color' delineation of bone microdamages using ligand-directed sub-5 nm hafnia nanodots and photon counting CT imaging," *Adv. Funct. Mater.*, vol. 30, no. 4, Jan. 2020, Art. no. 1904936.

[24] L. C. M. Lau, W. Y. W. Lee, A. P. H. Butler, A. I. Chernoglazov, K. Y. Chung, K. K. W. Ho, J. Griffith, P. H. Butler, and P. S. H. Yung, "Multi-energy spectral photon-counting computed tomography (MARS) for detection of arthroplasty implant failure," *Sci. Rep.*, vol. 11, no. 1, pp. 1–6, Dec. 2021.

[25] K. Baer, S. Kieser, B. Schon, K. Rajendran, T. ten Harkel, M. Ramyar, C. Löbker, C. Bateman, A. Butler, A. Raja, G. Hooper, N. Anderson, and T. Woodfield, "Spectral CT imaging of human osteoarthritic cartilage via quantitative assessment of glycosaminoglycan content using multiple contrast agents," *APL Bioeng.*, vol. 5, no. 2, Jun. 2021, Art. no. 026101.

[26] M. Moghiseh, C. Lowe, J. G. Lewis, D. Kumar, A. Butler, N. Anderson, and A. Raja, "Spectral photon-counting molecular imaging for quantification of monoclonal antibody-conjugated gold nanoparticles targeted to lymphoma and breast cancer: An *in vitro* study," *Contrast Media Mol. Imag.*, vol. 2018, pp. 1–9, Dec. 2018.

[27] M. Moghiseh *et al.*, "Cancer imaging with nanoparticles using MARS spectral scanner," in *Proc. IEEE Nucl. Sci. Symp. Med. Imag. Conf. (NSS/MIC)*, Nov. 2018, pp. 1–4.

[28] A. O. Gil, "Optimization of μCT imaging systems for soft-tissue dedicated tasks," Dept. de Bioingeniería e Ingeniería Aeroespacial, Carlos III Univ. Madrid, Getafe, Spain, Tech. Rep., 2019. [Online]. Available: http://hdl.handle.net/10016/28839

[29] J. M. D. S. E. Silva, I. Zanette, P. B. Noël, M. B. Cardoso, M. A. Kimm, and F. Pfeiffer, "Three-dimensional non-destructive soft-tissue visualization with X-ray staining micro-tomography," *Sci. Rep.*, vol. 5, no. 1, pp. 1–7, Nov. 2015.

[30] A. Ortega-Gil, J. J. Vaquero, M. Gonzalez-Arjona, J. Rullas, and A. Muñoz-Barrutia, "X-ray-based virtual slicing of TB-infected lungs," *Sci. Rep.*, vol. 9, no. 1, pp. 1–12, Dec. 2019.

[31] E. Hamann, T. Koenig, M. Zuber, A. Cecilia, A. Tyazhev, O. Tolbanov, S. Procz, A. Fauler, T. Baumbach, and M. Fiederle, "Performance of a Medipix3RX spectroscopic pixel detector with a high resistivity gallium arsenide sensor," *IEEE Trans. Med. Imag.*, vol. 34, no. 3, pp. 707–715, Mar. 2015.

[32] M. Moghiseh, "Optimization of spectral CT data acquisition for novel applications of nanoparticles, in radiology," Ph.D. dissertation, Dept. Radiol., Univ. Otago, Dunedin, New Zealand, 2018.

[33] R. Y. Chen *et al.*, "PET/CT imaging correlates with treatment outcome in patients with multidrug-resistant tuberculosis," *Sci. Transl. Med.*, vol. 6, no. 265, 2014, Art. no. 265ra166.

[34] A. Ortega-Gil, A. Muñoz-Barrutia, L. Fernandez-Terron, and J. J. Vaquero, "Tuberculosis histopathology on X ray CT," in *Image Analysis for Moving Organ, Breast, and Thoracic Images*. Cham, Switzerland: Springer, 2018, pp. 169–179.

[35] E. W. Tucker, B. Guglieri-Lopez, A. A. Ordonez, B. Ritchie, M. H. Klunk, R. Sharma, Y. S. Chang, J. Sanchez-Bautista, S. Frey, M. A. Lodge, S. P. Rowe, D. P. Holt, J. V. S. Gobburu, C. A. Peloquin, W. B. Mathews, R. F. Dannals, C. A. Pardo, S. Kannan, V. D. Ivaturi, and S. K. Jain, "Noninvasive ^{11}C-rifampin positron emission tomography reveals drug biodistribution in tuberculous meningitis," *Sci. Transl. Med.*, vol. 10, no. 470, Dec. 2018, Art. no. eaau0965.

[36] C. J. Bateman *et al.*, "MARS-MD: Rejection based image domain material decomposition," *J. Instrum.*, vol. 13, no. 5, May 2018, Art. no. P05020.

[37] S. Xu, P. Prinsen, J. Wiegert, and R. Manjeshwar, "Deep residual learning in CT physics: Scatter correction for spectral CT," in *Proc. IEEE Nucl. Sci. Symp. Med. Imag. Conf. (NSS/MIC)*, Oct. 2017, pp. 1–3.

[38] J. F. P. J. Abascal, N. Ducros, V. Pronina, S. Rit, P.-A. Rodesch, T. Broussaud, S. Bussod, P. C. Douek, A. Hauptmann, S. Arridge, and F. Peyrin, "Material decomposition in spectral CT using deep learning: A Sim2Real transfer approach," *IEEE Access*, vol. 9, pp. 25632–25647, 2021.

[39] A. M. Cadena, S. M. Fortune, and J. L. Flynn, "Heterogeneity in tuberculosis," *Nature Rev. Immunol.*, vol. 17, no. 11, pp. 691–702, Nov. 2017.

[40] S. D. Lawn, A. D. Kerkhoff, M. Vogt, and R. Wood, "Diagnostic accuracy of a low-cost, urine antigen, point-of-care screening assay for HIV-associated pulmonary tuberculosis before antiretroviral therapy: A descriptive study," *Lancet Infectious Diseases*, vol. 12, no. 3, pp. 201–209, Mar. 2012.

[41] A. A. Ordonez, M. A. Sellmyer, G. Gowrishankar, C. A. Ruiz-Bedoya, E. W. Tucker, C. J. Palestro, D. A. Hammoud, and S. K. Jain, "Molecular imaging of bacterial infections: Overcoming the barriers to clinical translation," *Sci. Transl. Med.*, vol. 11, no. 508, Sep. 2019, Art. no. eaax8251.

[42] C. A. Mutch, A. A. Ordonez, H. Qin, M. Parker, L. E. Bambarger, J. E. Villanueva-Meyer, J. Blecha, V. Carroll, C. Taglang, R. Flavell, R. Sriram, H. VanBrocklin, O. Rosenberg, M. A. Ohliger, S. K. Jain, K. D. Neumann, and D. M. Wilson, "[^{11}C] Para-aminobenzoic acid: A positron emission tomography tracer targeting bacteria-specific metabolism," *ACS Infectious Diseases*, vol. 4, no. 7, pp. 1067–1072, 2018.

[43] A. A. Ordonez, E. A. Weinstein, L. E. Bambarger, V. Saini, Y. S. Chang, V. P. DeMarco, M. H. Klunk, M. E. Urbanowski, K. L. Moulton, A. M. Murawski, S. Pokkali, A. S. Kalinda, and S. K. Jain, "A systematic approach for developing bacteria-specific imaging tracers," *J. Nucl. Med.*, vol. 58, no. 1, pp. 144–150, Jan. 2017.

[44] Z. Zhang, A. A. Ordonez, H. Wang, Y. Li, K. R. Gogarty, E. A. Weinstein, F. Daryaee, J. Merino, G. E. Yoon, A. S. Kalinda, R. C. Mease, J. N. Iuliano, P. M. Smith-Jones, S. K. Jain, and P. J. Tonge, "Positron emission tomography imaging with 2-[^{18}F] F-*P*-aminobenzoic acid detects staphylococcus *aureus* infections and monitors drug response," *ACS Infectious Diseases*, vol. 4, no. 11, pp. 1635–1644, 2018.

[45] P. L. Lin, T. Coleman, J. P. J. Carney, B. J. Lopresti, J. Tomko, D. Fillmore, V. Dartois, C. Scanga, L. J. Frye, C. Janssen, E. Klein, C. E. Barry, and J. L. Flynn, "Radiologic responses in cynomolgus macaques for assessing tuberculosis chemotherapy regimens," *Antimicrobial Agents Chemotherapy*, vol. 57, no. 9, pp. 4237–4244, Sep. 2013.

[46] L. E. Via, D. Schimel, D. M. Weiner, V. Dartois, E. Dayao, Y. Cai, Y.-S. Yoon, M. R. Dreher, R. J. Kastenmayer, C. M. Laymon, J. E. Carny, J. L. Flynn, P. Herscovitch, and C. E. Barry, "Infection dynamics and response to chemotherapy in a rabbit model of tuberculosis using [^{18}F]2-fluoro-deoxy-D-glucose positron emission tomography and computed tomography," *Antimicrobial Agents Chemotherapy*, vol. 56, no. 8, pp. 4391–4402, Aug. 2012.

[47] K. Lalwani, A. Giddabasappa, D. Li, P. Olson, B. Simmons, F. Shojaei, T. Van Arsdale, J. Christensen, A. Jackson-Fisher, A. Wong, and P. B. Lappin, "Contrast agents for quantitative microCT of lung tumors in mice," *Comparative Med.*, vol. 63, no. 6, pp. 482–490, 2013.

[48] E. Marfo, N. G. Anderson, A. P. H. Butler, N. Schleich, P. Carbonez, J. Damet, C. Lowe, J. Healy, A. I. Chernoglazov, M. Moghiseh, M. Collaboration, and A. Y. Raja, "Assessment of material identification errors, image quality and radiation doses using small animal spectral photon-counting CT," *IEEE Trans. Radiat. Plasma Med. Sci.*, early access, Jun. 18, 2020, doi: 10.1109/TRPMS.2020.3003260.